Space Weather

RESEARCH ARTICLE
10.1029/2018SW002004

Time Domain Simulation of Geomagnetically Induced Current (GIC) Flowing in 500-kV Power Grid in Japan Including a Three-Dimensional Ground Inhomogeneity

S. Nakamura[1], Y. Ebihara[1], S. Fujita[2,3], T. Goto[4], N. Yamada[1], S. Watari[5], and Y. Omura[1]

[1]Research Institute for Sustainable Humanosphere, Kyoto University, Kyoto, Japan, [2]Japan Meteorological Agency, Meteorological College, Kashiwa, Japan, [3]Space and Upper Atmospheric Research Group, National Institute of Polar Research, Tachikawa, Japan, [4]Graduate School of Engineering and Faculty of Engineering, Kyoto University, Kyoto, Japan, [5]National Institute of Information and Communications Technology, Tokyo, Japan

Key Points:
- Geoelectric field induced on the ground is calculated by time domain simulation with full 3-D ground conductivity
- GIC in Japanese 500-kV power grid is calculated and is found to be affected by localized geoelectric field and topology of power grid
- We simulate GIC for a moderate storm in May 2017, showing a certain agreement with the GIC observed at two substations in Japan

Correspondence to:
S. Nakamura,
satoko_nakamura@rish.kyoto-u.ac.jp

Citation:
Nakamura, S., Ebihara, Y., Fujita, S., Goto, T., Yamada, N., Watari, S., & Omura, Y. (2018). Time domain simulation of geomagnetically induced current (GIC) flowing in 500-kV power grid in Japan including a three-dimensional ground inhomogeneity. *Space Weather*, *16*, 1946–1959. https://doi.org/10.1029/2018SW002004

Received 5 JUL 2018
Accepted 15 OCT 2018
Accepted article online 25 OCT 2018
Published online 5 DEC 2018

Abstract We performed 3-D time domain simulation of geomagnetically induced currents (GICs) flowing in the Japanese 500-kV power grid. The three-dimensional distribution of the geomagnetically induced electric field (GIE) was calculated by using the finite difference time domain method with a three-dimensional electrical conductivity model constructed from a global relief model and a global map of sediment thickness. First, we imposed a uniform sheet current at 100-km altitude with a sinusoidal perturbation to illuminate the influence of the structured ground conductivity on GIE and GIC. The simulation result shows that GIE exhibits localized, uneven distribution that can be attributed to charge accumulation due to the inhomogeneous conductivity below the Earth's surface. The charge accumulation becomes large when the conductivity gradient vector is parallel or antiparallel to the incident electric field. For given GIE, we calculated the GICs flowing in a simplified 500-kV power grid network in Japan. The influence of the inhomogeneous ground conductivity on GIC appears to depend on a combination of the location of substations and the direction of the source current. Uneven distribution of the power grid system gives rise to intensification of the GICs flowing in remote areas where substations/power plants are distributed sparsely. Second, we imposed the sheet current with its intensity inferred from the ground magnetic disturbance for the magnetic storm of 27 May 2017. We compared the calculated GICs with the observed ones at substations around Tokyo and found a certain agreement when the uneven distribution of GIE is incorporated with the simulation.

1. Introduction

Geomagnetically induced current (GIC) is hazardous to social infrastructures having long-length conductors such as power lines, pipelines, and communication cables. One of the most famous consequences is the collapse of the Hydro-Québec power grid on 13 March 1989 associated with a severe geomagnetic storm (Boteler, 2001; Boteler et al., 1989; Kappenman, 1989). When the surface electric field, called a geomagnetically induced electric field (GIE), arises (Boteler, 2001), GIC flows in grounded conductors. The time-varying magnetic field associated with electric currents flowing in the magnetosphere and/or the ionosphere induces GIE. It is known that GIE increases with magnetic activities, such as magnetic storms and/or substorms (Pulkkinen et al., 2008). Thus, the risk is expected to be higher for larger magnetic storms and substorms.

Change in the geomagnetic field $\partial B/\partial t$ is used as a proxy for GIE, which is significantly stronger at higher geomagnetic latitude (MLAT) due to an auroral current system (e.g., Pulkkinen et al., 2012). GIE is expected to be smaller in magnitude below 50° MLAT than at higher MLAT, where MLAT stands for magnetic latitude. Therefore, it has been believed that the occurrence of strong GICs is limited in the high latitude regions (Thomson et al., 2011). In fact, blackouts of power systems due to GIC have been experienced in North America and Scandinavia (Bolduc, 2002; Pulkkinen et al., 2005; Wik et al., 2008). The four main Japanese Islands belong to the low- and midlatitudes (<~37° MLAT) where the influence of the auroral electrojet is believed to be most likely negligible. For example, Takasu et al. (1994) noted that the influence from GIC on the Japanese power grid would be quite limited because excess heat excited by GIC at the transformer could be limited and the occurrence frequency of large amplitude GICs was low. However, recently, it has been suggested that the Japanese grid system may not be always safe as previously thought. That is to say, the intensity of GIC flowing in Japan is roughly proportional to $|Dst|$, and it could reach levels of 100 A for large magnetic storms such as the storm of 13–14 March 1989 (Kappenman, 2004). Indeed, unusually

large-amplitude GIC with about 130 A was measured in Japan in the October 2003 storm (Ministry of Economy, Trade and Industry of Japan, 2015). Unfortunately, the place of the measurement is still undisclosed. Although this large GIC caused no damages to the transformer in Japan at that time, there are several reports of thermal damage of transformers by GICs at geomagnetically low- and midlatitudes such as South Africa (Gaunt & Coetzee, 2007), New Zealand (Béland & Small, 2004), and China (Liu et al., 2009; Liu & Xie, 2005). Under such circumstances, one cannot say that low- and midlatitude regions are safe against GICs. We need to evaluate the GIC risk quantitatively to prepare for upcoming severe space weather disasters (Tsurutani et al., 2003; Watari et al., 2001).

GIC at low- and midlatitudes is probably related to the magnetic disturbances associated with magnetic storms (Kappenman, 2004). A spike-like large-amplitude variation of the geomagnetic field is recorded at low-latitude during the initial phase of a magnetic storm (e.g., Araki, 2014). This is known as a sudden commencement and is caused by the sudden compression of the magnetosphere. The amplitude of the *H* component larger than 273 nT was recorded at Kakioka (KAK), Japan, in 1940 (Araki, 2014). During storm's main and recovery phases, the *H* component of the geomagnetic field shows a negative excursion lasting for a few days. The magnetic depression is primarily caused by the intensification of the ring current. For example, a large-amplitude magnetic depression with an amplitude of ~600 nT was observed at KAK on 13 March 1989 (Walker & Wong, 1993). Ionospheric current associated with the DP2 current system is probably not negligible at midlatitude as pointed out by Tsurutani et al. (2005). The ionospheric current is enhanced almost simultaneously from the pole to the equator in response to the variation of the interplanetary magnetic field (Kikuchi et al., 1996; Kobea et al., 2000; Nishida, 1968). During magnetic storms, the auroral oval expands to lower latitudes (e.g., Yokoyama et al., 1998). The equatorward boundary of the auroral oval expanded to ~40° MLAT during the 13–15 March 1989 storm (Yokoyama et al., 1998). If auroral electrojets are accompanied with the auroral oval, the auroral electrojets may have some influence on the midlatitude GIC for extreme magnetic storms.

Many investigations of GIE have employed uniform or one-dimensional (1-D) conductivity models and assumed plane wave incident on the ground (Kappenman, 2004; Liu et al., 2014; Marshall et al., 2017; Viljanen & Pirjola, 1989; Weigel & Baker, 2003). The assumption relies on the idea that small-scale inhomogeneities in the ground conductivity do not significantly affect the large-scale distribution of GIE (e.g., Cagniard, 1953). When the inhomogeneities are nonnegligible, the incident electric field results in charge accumulations in localized regions, which are associated with higher magnitude localized electric field. This situation will be significant in the region where the ground conductivity is complicated. The Japanese islands are surrounded by the high-conducting sea with a coastal topography that is quite complex and steeply shelving near the shore. Under Japan, the ground structures are known to be complicated, including sediment layers, partial melts beneath volcanoes, and subduction zone hydration. That is because Japan is located in a plate boundary region with four tectonic plates. This combination of coast lines and ground structures will make the GIE distribution complicated as demonstrated with simple conductivity models by Goto (2015). Using a thin heterogeneous surface shell and a layered 1-D structure underneath (e.g., Kuvshinov, 2008; Püthe & Kuvshinov, 2013; Püthe et al., 2014), Püthe et al. (2014) have shown the complicated distribution of GIE in Japan. The calculated GIE shows a good agreement with the GIE acquired at 3 observatories in Japan and 4 ocean bottom observatories. With the 3-D forward solver of finite difference methods developed by Mackie et al. (1994) and Uyeshima and Schultz (2000), Fujita et al. (2018) solved the electromagnetic induction of a spherical Earth in the frequency domain by using a 3-D model of ground conductivity with a resolution of the order of tens of km. They introduced a ring-shaped external source current with its intensity changing at periods of 200, 800, and 3,600 s. The result also shows the fine-scale distribution of GIE in Japan. With a full 3-D conductivity model, Honkonen et al. (2018) solved the world-wide distribution of GIE. They used a global magnetohydrodynamics simulation result as a source current. Ivannikova et al. (2018) also employed the full 3-D conductivity model and calculated time variation of GIE in Ireland. Previous studies have suggested that the overall distribution of GIE in the Japanese islands is probably similar to that of New Zealand (Divett et al., 2017), Ireland (Blake, 2017), and UK (Beggan et al., 2013) because the Japanese islands are also surrounded by deep sea.

Our focus is on the global distribution of GIC calculated using the time domain calculation of electric and magnetic fields. We employed the 3-D finite-difference time domain (FDTD) method (Taflove, 1980; Yee, 1966) to calculate the GIE. The FDTD method solves the Maxwell equations directly. One of the advantages

of the use of the FDTD method is to calculate the temporal variation of the electromagnetic fields in the time domain. This means that our method is different from that used by Fujita et al. (2018), who solved the Maxwell equation in the frequency domain. This also means that we can calculate the temporal variation of GIE without performing the inverse Fourier transformation (e.g., Marshall et al., 2017; Püthe et al., 2014), or applying the convolution theorem (e.g., Kelbert et al., 2017). The purpose of this paper is to show the influence of the inhomogeneous ground conductivity on GIC flowing in Japan on the basis of the GIE obtained by the FDTD method together with the realistic, inhomogeneous, and 3-D model of the ground conductivity. As far as we surveyed, this is the first study that models the global distribution of the GIC flowing in the Japanese power grid from the Hokkaido island (northernmost main island) to the Kyushu island (southernmost main island). Kappenman (2004) modeled the regional distribution of the GIC in central Japan (a part of the Honshu island) only. Pulkkinen et al. (2010) calculated the GIC at a substation in the Hokkaido island by computing a system parameter to relate GIC and GIE.

This paper is organized as follows. In section 2, we explain settings and assumptions of our model. In section 3, we present the initial result of our simulations for two source currents. One is the sheet current that varies in a sinusoidal manner in time. The other is the sheet current that varies in a manner inferred from the observed magnetic disturbance time series. We compare the simulation results with the observations made at substations. Finally, we discuss the results in section 4.

2. Model

The calculation consists of two steps. In the first step (geophysical step), we determined the horizontal component of GIE on Earth's surface as functions of space and time. In the second step (engineering step), we calculated GIC flowing in the power grid for the GIE obtained in the first step.

2.1. Geophysical Step

2.1.1. Evolution of Electric Field and Magnetic Field

We applied the 3-D FDTD method (Taflove, 1980; Yee, 1966) to model the electrodynamics of the complete Earth-ionosphere system. The FDTD method solves Maxwell's equations directly in time domain. The time variation of the magnetic and electric fields is directly obtained without the inverse Fourier transform.

Maxwell equations used by the FDTD method are

$$\nabla\times\boldsymbol{E} = -\frac{\partial \boldsymbol{B}}{\partial t} \tag{1}$$

and

$$\nabla\times\boldsymbol{B} = \mu_0\boldsymbol{j}_s+\mu_0\sigma\boldsymbol{E} + \mu_0\epsilon_0\frac{\partial \boldsymbol{E}}{\partial t}. \tag{2}$$

where $\boldsymbol{E}$, $\boldsymbol{B}$, $\boldsymbol{j}_s$, μ_0, ϵ_0, and σ are the electric field, the magnetic field, the source current density, the magnetic permeability, the permittivity in vacuum, and the conductivity, respectively. The permittivity and permeability were assumed to be the same as in free space. The conductivity depends on the location as described below. The standard Cartesian Yee lattice (Yee, 1966) is applied, in which the electric field components are stored on cell edges, while the magnetic field components are stored on the corresponding face centers. With finite differentiations, (1) and (2) turn into

$$E_k^n = \frac{1-\frac{\sigma\Delta t}{2\epsilon_0}}{1+\frac{\sigma\Delta t}{2\epsilon_0}}E_k^{n-1} + \frac{\frac{\Delta t}{\mu_0\epsilon_0}}{1+\frac{\sigma\Delta t}{2\mu_0\epsilon_0}}\left(\frac{\partial H_j^{n-\frac{1}{2}}}{\partial x_i}-\frac{\partial H_j^{n-\frac{1}{2}}}{\partial x_j}\right) \tag{3}$$

and

$$B_i^{n+\frac{1}{2}} = B_i^{n-\frac{1}{2}} - \Delta t\left(\frac{\partial E_k^n}{\partial x_j}-\frac{\partial E_j^n}{\partial x_k}\right), \tag{4}$$

respectively. The superscript means time step, and the subscripts (i,j,k) mean (x,y,z) or (y,z,x) or (z,x,y). The simulation grid covers the region ranging from 25° to 50° latitude and from 125° to 150° longitude with a

10-km horizontal grid spacing and ranging from −100 to 100 km altitude with 0.1-km vertical spacing. The horizontal scale of each grid corresponds to ~0.1° × ~0.1° latitude-longitude grid size around Japanese islands. The time step was set to 10^{-5} s. The Berenger perfectly matched layer absorbing-boundary condition (Berenger, 1994) was applied to avoid unwanted reflection at the boundary of the simulation box.

2.1.2. Source Current Model

A uniform sheet current flowing at 100-km altitude is imposed on the FDTD simulation to excite the electric and magnetic fields. First, we change the current density sinusoidally in time. The *x* component (geographical northward) and *y* component (geographical eastward) of the current density are given by

$$J_x(t) = -J_s \cos\left(\frac{2\pi}{T}t\right) \sin\theta, \tag{5}$$

$$J_y(t) = J_s \cos\left(\frac{2\pi}{T}t\right) \cos\theta, \tag{6}$$

where J_s is the maximum intensity of the source current, t is time, T is period, and θ is angle from east (positive clockwise). J_s and T are assumed to be 0.02 A/m and 100 s, respectively. This sheet current induces a magnetic field on the ground of the order of 10 nT, which is a typical amplitude for a sudden commencement invoked by a solar wind shock. The amplitude and frequency are arbitrary chosen but are not far from the reality. We changed the direction of the source current from $\theta = 0°$ (east-west direction) to 90° (north-south direction).

We also change the current density in accordance with the geomagnetic variation on the ground. Assuming an infinitely extended horizontal current, we obtained the current density on the basis of the Ampère's law (Kamide & Brekke, 1975) as

$$J_x(t) = -\alpha \frac{2}{\mu_0} \Delta B_y', \tag{7}$$

$$J_y(t) = \alpha \frac{2}{\mu_0} \Delta B_x', \tag{8}$$

where μ_0 is the magnetic permeability, $\Delta B_x'$, is the magnetic disturbance in the *x* direction, $\Delta B_y'$ is the magnetic disturbance in the *y* direction, and α is a factor associated with induction and the effect of deviation from the horizontal current and the ground of the Earth. We assumed α to be 1/1.5 (Kamide & Brekke, 1975). It should be noted that for the low-frequency variation of the source current, the incident electric field $\boldsymbol{E}_0$ just above the ground is oriented to the opposite direction of the source current $\boldsymbol{J}_s$ as shown in Appendix A.

2.1.3. Conductivity Model

Following Fujita et al. (2018), we divided the 3-D simulation domain into the following four regions: the air, the seawater, the sediment layer, and the basement rock layer. The two published data, the ETOPO1 (Amante & Eakins, 2009) Global Relief Model from the National Centers for Environmental Information, the National Oceanic and Atmospheric Administration (https://ngdc.noaa.gov/mgg/global/global.html), and a global digital map of sediment thickness (Laske & Masters, 1997) were used to determine the regions. The data were linearly interpolated to fit the grid used by the FDTD method. We assumed the electric conductivities of the air, the seawater, the sediment layer, and the basement rock layer to be 0, 2.5, 10^{-2}, and 10^{-3}, respectively. The full 3-D distribution of the conductivity is applied to solve equation (2). Thin-sheet assumption is unnecessary because we solved the evolution of the electric field and the magnetic field in the 3-D space directly.

Figure 1a shows the relief map of the modeled region. A complex submarine topography is present around Japan. The main Japanese islands are located on the continental shelf. There is a deep-sea ocean in the east direction of them. On the other hand, a relatively shallow sea depth less than 1 km extends in the west direction of it. Figure 1b shows the thickness of the sediment layer. On average, the main Japanese islands have a 0.2–0.4 km thickness of sediment layers, except for some anomalies. The sediment layer is rather thick in the north part of Japan (a part of the Hokkaido island, Figure 2), west Tohoku and east Kanto areas. Figure 1c shows the resistivity (which is the inverse of the conductivity) averaged over the top 2 km beneath the ground.

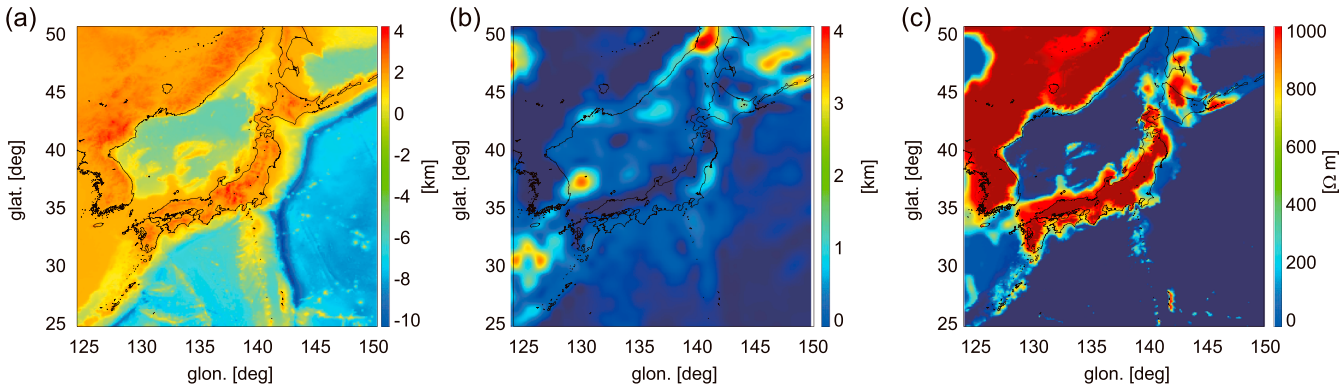

Figure 1. (a) The ETOPO1 global relief model from the National Oceanic and Atmospheric Administration/National Centers for Environmental Information, (b) the sediment thickness model derived by Laske and Masters (1997), and (c) the resistivity averaged over the top 2 km beneath the ground.

2.2. Engineering Step

The GIC flowing in the Japanese power grid was calculated using the method derived by Lehtinen and Pirjola (1985). We treated the GIC as a DC current because the frequencies of GIC are much lower than those of the power line of 50 and 60 Hz. Using publicly available information, we constructed a simplified model of 500-kV power grid that consists of 134 nodes and 160 links as shown in Figure 2. Five hundred kilovolt is the highest class in the commercial power grid in Japan. We assume the conductivity of lines based on public relations materials by Tokyo Electric Power Company Power Grid, Incorporated. The assumptions that we made are as follows: (1) All the power lines have a constant cable resistance per unit length of 1.43×10^{-6} Ω/m except for the lines designed for the ultrahigh voltage of 1,000 kV. The cable resistance per unit length of 9.42×10^{-7} Ω/m was applied for the lines designed for the ultrahigh voltage of 1,000 kV, which is shown in the thick lines in Figure 2. (2) Both the earthing resistance and the winding resistance are assumed as 0.05 Ω. This value is arbitrary chosen and is probably very low in comparison with other transformers and Earth ground resistances. We will improve this value in the future. (3) Due to historical reasons, the power-line network in Japan is divided in two parts in terms of utility frequency. The frequency is 50 Hz in the east part of Japan and 60 Hz in the west part. We assumed that GIC does not flow through the frequency converter station that faces the 50-Hz power lines and 60-Hz power lines. (4) The voltage between two points (substations/power plants) were calculated by integrating the electric field along the great circle between them.

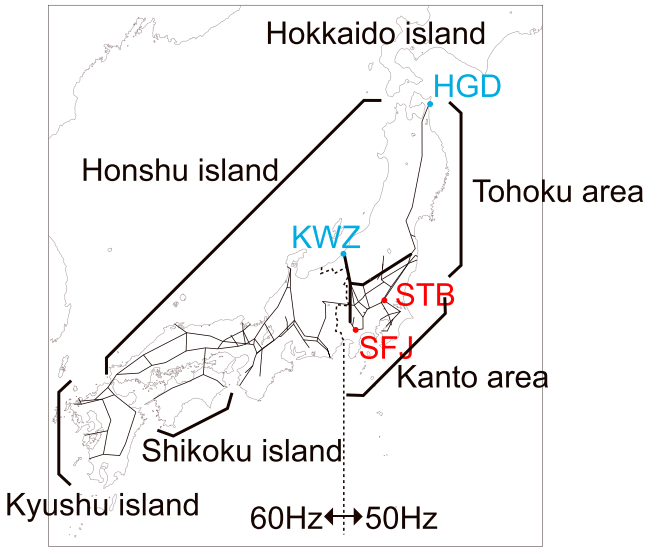

Figure 2. Simplified model of the Japanese 500-kV power grid. The thick lines indicate the power lines designed for the ultrahigh voltage of 1,000 kV. The measurement of geomagnetically induced current has been conducted at the Shin-Tsukuba and Shin-Fuji substations. The dashed line is the boundary of utility frequencies between 50 and 60 Hz.

As shown in Figure 2, the density of the power lines and substations/power plants is uneven because of a great demand in urban areas. The number of substations/power plants is higher in urban areas, for example, Tokyo metropolitan area in Kanto, than in remote areas. Most of endpoints of the power lines are located near the seashore, for example, Higashidori and Kashiwazaki (KWZ).

2.3. Observation

We compare the calculated magnetic field, electric field, and GIC with observed ones. We use the 1-Hz magnetic field and electric field data from Memambetsu (MMB) located at 43.91°N, 144.19°E in the Hokkaido island, KAK located at 36.23°N, 140.19°E in the Kanto area, and Kanoya (KNY) located at 31.43°N, 130.88°E in the Kyushu island. Triaxial high-sensitivity fluxgate magnetometers are used to observe the magnetic field. The accuracy is 0.01 nT. The data are certified as INTERMAGNET observatories. A pair of the north-south (NS) line and east-west (EW) line with copper plates is used to observe the electric field. The NS and EW lines are located orthogonally. The lengths of the NS and EW lines are (300 m, 300 m), (180 m,

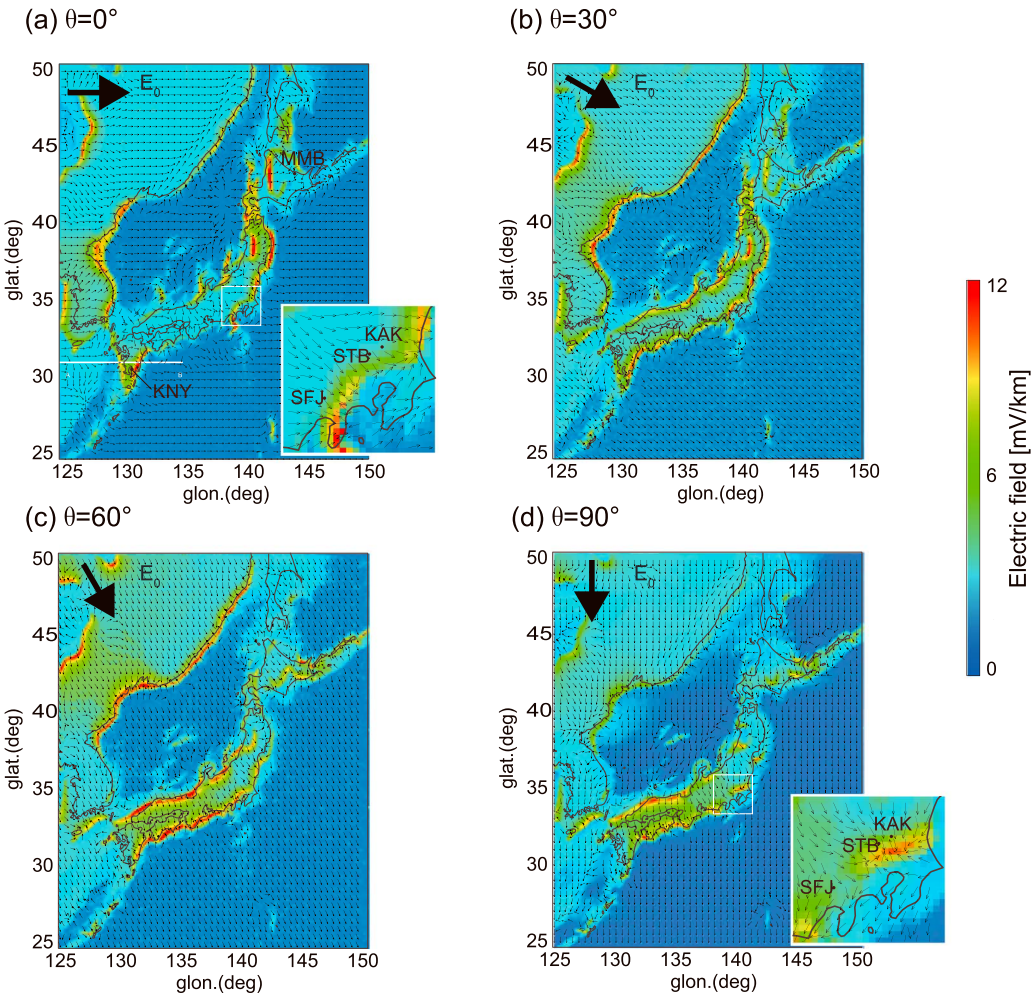

Figure 3. Magnitude of geomagnetically induced electric field (GIE) at the surface of the ground at t = 50 s for (a) θ = 0° (incident electric field E_0, meaning the primary electric field propagated from the ionosphere, directed eastward), (b) θ = 30°, (c) θ = 60°, and (d) θ = 90° (E_0 directed southward). MMB, KAK, and KNY stand for Memambetsu, Kakioka, and Kanoya observatories (see text). The direction of GIE is drawn by the small black arrows. The large black arrows at the top-left corners of panels show the directions of E_0 on the ground. Enlarged views of the Kanto area are presented in (a) and (d).

190 m), and (200 m, 200 m) at MMB, KAK, and KNY, respectively. The detailed information about the observatory is provided by Minamoto (2013) and the Web http://www.kakioka-jma.go.jp/obsdata/metadata. To measure GIC, a clamp type ammeter (Hioki E. E. Corporation, product number of 9272) is attached to a neutral line of one of the multiple transformers at the STB and SFJ substations as shown in Figure 2. The ammeter employs an InSb Hall sensor element. The accuracy of the amplitude is ±0.5% in the frequency range from DC to ~1 kHz. The temperature characteristics of the sensor are ±0.05%/K in amplitude and ±0.005%/K in offset. The sampling rate is 10 Hz. All data are smoothed for comparison with a 1-min running average. The smoothing is required to avoid numerical problems in the computation, although the smoothing is expected to cause the underestimation of GIE and GIC. We will overcome this problem in the future.

3. Results

3.1. Sinusoidally Varying Source Current

Figures 3a–3d summarize the magnitude of GIE induced at the surface of the ground at t = 50 s when the incident electric field E_0 is maximized for θ = 0°, 30°, 60°, and 90°. The source current varies at 100-km altitude sinusoidally with a period of 100 s. At t = 50 s (at a half cycle), the source current is directed to westward for

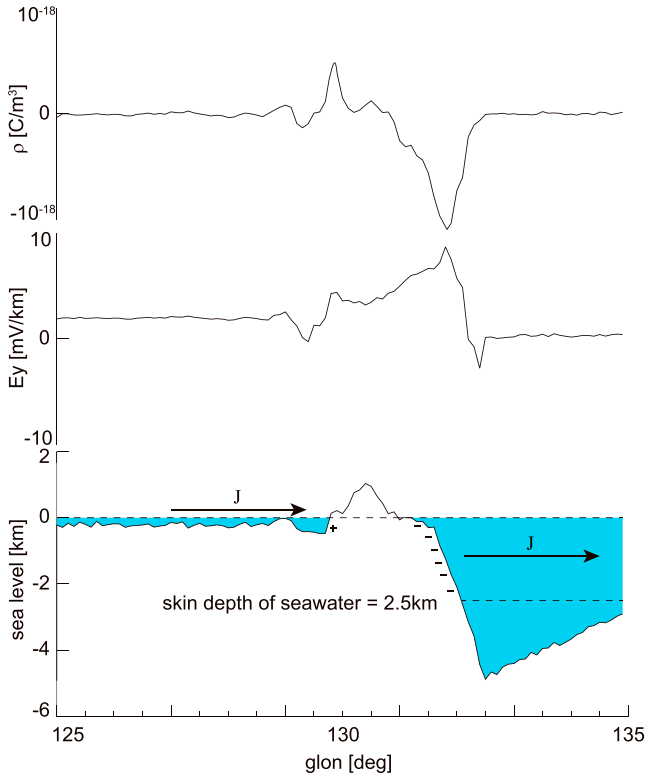

Figure 4. (top) Charge density, (middle) eastward electric field on the ground, and (bottom) sea level along the cross section of the Kyushu area at $t = 50$ s. They are taken along the white line drawn in Figure 3a. The charge density ρ is calculated by $\rho = \varepsilon_0$ div **E**, where ε_0 is the electric permittivity and **E** is the electric field. In the bottom panel, the symbols "+" and "−" stand for positive and negative electric charge, respectively.

$\theta = 0°$ and northward for $\theta = 90°$. The calculated GIE shows an uneven distribution, resulting from the inhomogeneities of the ground conductivity. The magnitude of the GIE in the deep offshore regions is relatively smaller than onshore regions. In particular, large GIE appears in the onshore region where the coast lines are normal to incident electric field. The overall magnitude of GIE on the ground is larger than 2.5 mV/m in the main Japanese island, whereas the overall magnitude is less than 1 mV/m on the Pacific Ocean.

In general, the localized, uneven distribution of the GIE is attributed to charge accumulation that occurs when the conductivity gradient is parallel to the direction of the incident electric field. One such effect is called a coastal effect (Mckay & Whaler, 2006; Parkinson & Jones, 1979). For $\theta = 0°$, the incident electric field E_0 is directed eastward at $t = 50$ s, and the GIE is locally enhanced near the east and west coast lines in Tohoku area. In addition to the coastal effect, the GIE is also enhanced around the inhomogeneities of the relatively highly conductive sediment layers in Hokkaido, the Tohoku, and the Kanto areas by the high local conductance of the sediment. A similar effect was noted in New Zealand's sediment regions by Divett et al. (2017). The GIE directs southeastward or northwestward in the main island of Japan independently of the direction of the incident electric field. This is the normal direction to the main axis of the main Japanese island. The magnitude of the GIE is most enhanced when the incident magnetic field is normal to the coast line.

Enlarged figures of GIE in the Kanto area are shown in Figures 3a and 3d to highlight the locally enhanced and strongly distorted electric field in the inland area of Kanto. There is an anomaly zone of a thick sedimentary layer in the Kanto area. The electric field is enhanced in the region where the gradient of conductivity is large. This feature is consistent with reports of an unusually large amplitude of short-period geomagnetic variation, which is called the "Kanto anomaly" (Honkura, 1985). In the Kanto area, GIE is highly distorted. For example, GIEs at the two substations STB and SFJ are quite different from each other in terms of magnitude and direction, although the distance between the two substations is only about 100 km. In Kyushu island, the GIE enhancement is larger in the east coast than in the west coast because the continental shelf between China and the Kyushu area weakens coastal effects. The cross section of the Kyushu area is shown in Figure 4. It is clearly shown that the west coast of the Kyushu island faces a shallower seafloor (the East China Sea) and has smaller charge accumulation than that of the east coast facing a deep ocean (the Pacific Ocean). The skin depth of seawater is approximately 2.5 km for the incident electromagnetic field with a period of 100 s in the seawater (2.5 S/m). Because the skin depth of the incident plane waves is longer than the sea depth in the East China Sea, the electric field penetrates deeper into the seafloor on the shallower sea on the west side of Kyushu than on the east side. This results in relatively smaller GIE on the west side than on the east side.

For $\theta = 60°$, the incident electric field E_0 is directed from northwest to southeast. Figure 3c clearly indicates that GIE is intensified in the region where the coast line is perpendicular to E_0. This is consistent with the result by Divett et al. (2017), who pointed out that GIE is intensified in the region where a disturbed magnetic field is aligned parallel to the main axis of the islands (a disturbed electric field is aligned perpendicular to the main axis of them.

For $\theta = 90°$, the incident electric field E_0 is directed southward at $t = 50$ s. The GIE is locally enhanced near the southern part of Shikoku island, and the northwest part of Honshu island (Figure 2). The coastal effect is more pronounced near a curved shoreline such as a cove, a bay or a gulf. Roughly speaking, the main Japanese islands are approximately distributed along a large arc with a center located in the northwest of them. The strong induced current in the west and north coasts of the main Japanese islands is found along the coast line of the Sea of Japan, resulting in the large GIE along the northwest coast of Japan. The local enhancement

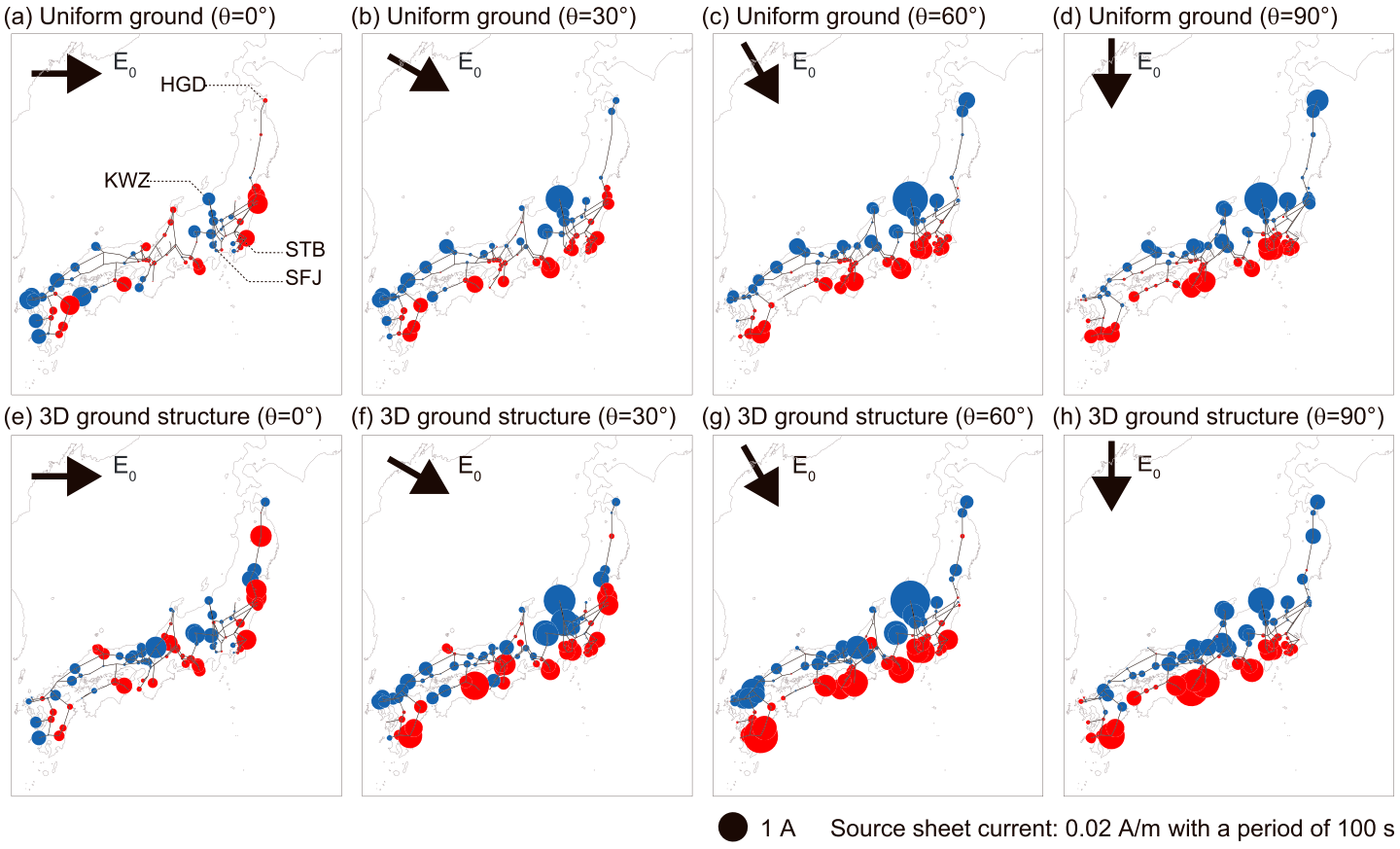

Figure 5. (top) Geomagnetically induced current (GIC) flowing between the ground and the power grid for a uniform, steady geomagnetically induced electric field (GIE) directed at (a) 0° (eastward), (b) 30°, (c) 60°, and (d) 90°(southward). (bottom) GIC for the GIE calculated by the 3-D finite-difference time domain model for the direction of the source sheet current at (e) 0° (westward), (f) 30°, (g) 60°, and (h) 90°(northward) at t = 50 s as shown in Figure 3. The radius of the circles is proportional to the magnitude of GIC flowing to/out of the ground. The blue and red colors indicate GIC flowing into the grid and out of the grid, respectively. The thick black arrow in the top-left corner in panel shows the direction of the incident electric field E_0 on the ground.

of GIE is pronounced in the west-north coast of Honshu island for θ = 30° and 60°. Note that the GIE shown in Figure 3 is locally distorted to the incident electric field in the Kanto area by the inhomogeneities of the ground conductivity.

Figure 5 presents the distribution of GIC flowing between the modeled power grid and the ground. In Figures 5a–5d, we present GIC calculated with a uniform, steady GIE with an amplitude corresponding to the incident electric field (from eastward to southward) at t = 50 s when the incident electric field is maximized. The distribution of GIC is largely influenced by the topology of the network of the power grid. This is consistent with the results by Beggan (2015) and Divett et al. (2017). The calculated GIC tends to be enhanced at most of the end points of the power grid, for example, Higashidori and KWZ, depending on the direction of the incident electric field, or the direction of the source current. The two stations are pointed by dashed lines in the Figure 5a. For the eastward GIE (angle of 0°), GIC tends to flow into the power grid in the west part and out of the grid in the east part of each island. An interesting point is that the GIC is relatively small in the Tohoku area, although the Tohoku area has a large GIE as shown in Figure 3b. This is probably due to the situation that the power line is almost orthogonal to the direction of the GIE. For the southward GIE (angle of 90°), GIC tends to flow into the power grid in the north part, and out of the grid in the south part of each island.

In case of the uniform GIE, the magnitude of GIC is largest at KWZ, which is caused by the uneven distribution of substations/power plants. KWZ is a power plant, which is isolated from the Tokyo metropolitan area where a number of grounded substations are situated. Most of the GIC flowing out from the grid in the Tokyo

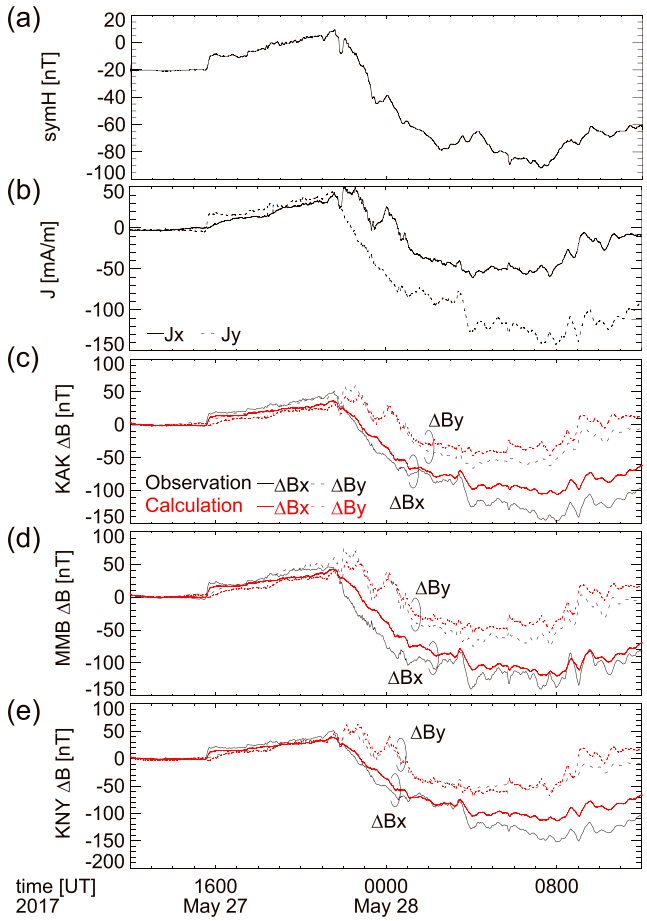

Figure 6. (a) The sym-H index, (b) *x* and *y* components of averaged current density of the sheet current that is assumed to flow at 100-km altitude, and (c–e) *x* and *y* components of the magnetic field at KAK, MMB, and KNY.

metropolitan area is thought to be supplied from KWZ. KWZ is located in the north direction of Tokyo metropolitan area, so that the effects by uneven distribution of substations/power plants expected to maximize the GIC when the NS electric field is imposed on the ground. In addition, the power line connected to KWZ is designed for the ultrahigh voltage of 1,000 kV (as indicated by the thick line in Figure 2); that is, the cable resistance of the power line is lower than the other power lines in this study. This may also enhance the GIC at KWZ.

Figures 5e–5h show GIC calculated with GIE obtained by the 3-D FDTD method with the inhomogeneous ground conductivity. For the incident electric field with angles equal to, or larger than 30°, GIC tends to be enhanced, in particular, in the south and north-west part of the main Japanese islands. This is due to the GIE enhanced by the coastal effect in association with the curved coast line as shown in Figure 3. In addition, the local enhancement of GIC can be seen (e.g., the Tohoku area in Figure 5e). Thus, the uneven distribution of GIE introduced by the inhomogeneous ground conductance results in the both regional and local enhancements of GIC at many points, especially located near seashore.

3.2. Realistic Source Current Variation

For a more realistic case study, we employed a sheet current with an amplitude estimated from the ground magnetic disturbance to demonstrate a temporal variation of GIC during the magnetic storm occurred on 27–28 May 2017. Figure 6a shows the sym-H index (Iyemori, 1990), indicating that a moderate storm occurred with a sudden commencement. The storm sudden commencement occurred at 1530 UT, which is caused by the enhancement of the magnetopause current. The storm main phase might start at around 2130 UT. The storm main phase lasted for about 10 hr, which is most likely attributed to the enhancement of the ring current. The magnetopause current usually flows at >10 Earth radii, and the ring current usually flows at 2–7 Earth radii. The procedure to obtain GIC is as follows: (1) We calculated the sheet current density on the basis of the geomagnetic field variation at three observatories. (2) With the calculated sheet current, we performed the FDTD simulation to obtain GIE on the surface. (3) With the GIE, we calculated GIC by using the power grid model.

The first step is to estimate the source current flowing over Japan. It is reasonable to consider that the source current is a uniform sheet current extending to infinity because the scale length of the main Japanese islands is much smaller than the characteristic scale lengths of the magnetopause current and the ring current. The amplitude and direction of the sheet current are estimated by the following procedure. First, we subtract the ground magnetic fields observed by Japan Meteorological Agency at MMB, KAK, and KNY from those values observed at 1200 UT on 27 May 2017. We call them $\Delta\mathbf{B}_{MMB}(t)$, $\Delta\mathbf{B}_{KAK}(t)$, and $\Delta\mathbf{B}_{KNY}(t)$, respectively. The black lines in Figures 6c–6e show $\Delta\mathbf{B}$ at KAK, MMB, and KNY. Second, we calculate the average of the magnetic fields observed at the 3 observatories. That is, $\Delta\mathbf{B}(t) = (\Delta\mathbf{B}_{MMB}(t) + \Delta\mathbf{B}_{KAK}(t) + \Delta\mathbf{B}_{KNY}(t))/3$. Third, we apply a low-pass filter to remove a high frequency component (>1/100 Hz) of the magnetic field. We call this $\Delta\mathbf{B}'(t)$. Fourth, we calculate the current density by using (7) and (8). Figures 6b and 6c show the current density of the sheet current in the *x* (north) and *y* (east) components. Obviously, the current in the *y* component dominates that in the *x* component. The dominance of the *y* component may imply the significant contribution from the ring current flowing westward and the magnetopause current flowing eastward. The current in the *x* component is nonnegligible, suggesting the contribution from the ionospheric current and/or the field aligned current flowing in the higher latitude region.

The second step is to calculate the GIE excited by the source current. The FDTD simulation provides the electric field and the magnetic field in the simulation domain. Figures 6c–6e show the observed and

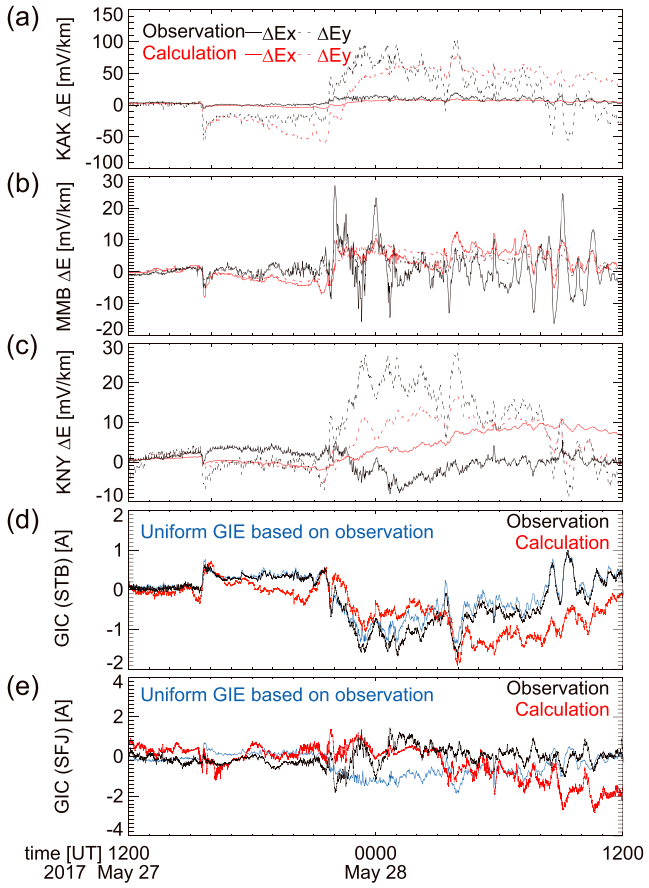

Figure 7. (a–c) Electric field on the ground observed at KAK, MMB, and KNY and (d and e) geomagnetically induced current (GIC) at the STB and SFJ substations. The black line indicates the observed value, and the red line indicates the one obtained by the finite-difference time domain simulation. In Figures 7d and 7e, the blue line indicates the calculated GIC with a uniform GIE observed at KAK.

calculated magnetic fields at three stations. The red lines show the simulated ones, indicating a fairly good agreement with the observation indicated by the black lines. However, there is a tendency that the calculation is underestimated a bit in comparison with the observation. This difference may come from the overestimation of the α value used to estimate the source current. The α value should include information about the ground conductivity and should depend on frequency of the incident electric field. The α value should be consistent with the assumed ground conductivity. The assumption of the uniform source current may also cause the difference. We will incorporate more realistic source current model and investigate the difference in the near future. Figures 7a–7c show the electric field on the ground observed at KAK, MMB, and KNY. Again, we subtract the electric fields from those values observed at 1200 UT on 27 May 2017 and call them $\Delta\mathbf{E}_{MMB}(t)$, $\Delta\mathbf{E}_{KAK}(t)$, and $\Delta\mathbf{E}_{KNY}(t)$, respectively. The red lines show the simulated ones. A certain agreement with the observation is also found except for short-time fluctuations (less than 1 hr). The short cycle fluctuation of the calculated electric field hardly reproduces the observed one. This is probably due to the ground conductivity that is not considered by our model.

The final step is to calculate the GIC. Figures 7d and 7e show the temporal variation of the GIC flowing between the power grid and the ground at the STB and SFJ substations, respectively. The substations are located in the Kanto area and are indicated in Figure 2. The red lines and black lines indicate the simulated GIC and the observed GIC, respectively. The GIC observed at the STB and SFJ substations is the current flowing in a neutral line between a single transformer and the ground. Since GIC flowing in the power line splits into transformers at a substation, we need to divide the calculated GIC by the number of the substations. The number of the transformers is not open to public, so that we simply assume that the number of the transformers is 10. There are tendencies in Figures 7d and 7e that the GIC variation at the STB substation is inversely proportional to the *y* component of the electric field, whereas the GIC variation at the SFJ substation seems to be influenced by the both components of the electric field. An interesting point is that the variation at SFJ is completely different from that at STB, although the distance between the two substations is about 120 km. The blue line in Figures 7d and 7e indicates the calculated GIC with the uniform GIE that is the same as that observed at the KAK observatory, while the red line indicates the calculated GIC with the GIE that comes from the FDTD method. When the uniform GIE is applied, the calculated GIC at STB is similar to the observed one because STB is close to the KAK observatory. However, the calculated GIC at SFJ is completely different from the observation. This most likely implies that the localized distribution of the GIE (as shown in Figure 3) arising from the inhomogeneities in the ground conductivity largely influences the GIC variation. Of course, the geometry of the power grid also results in the difference between STB and SFJ.

4. Discussion and Conclusions

The electric field on the ground was derived from the 3-D FDTD method with the full 3-D ground conductivity model. It is clearly demonstrated by the FDTD simulation that the uneven distribution of GIE is attributed to charge accumulation, which occurs significantly when the conductivity gradient is parallel to the incident electric field. Air, sea, sediment layers, and rock layers are only considered, while effects of other ground structures, such as sediment layers, partial melts beneath volcanoes, and subduction zone hydration, are not taken into consideration. In spite of the simple ground conductivity model, the calculated GIE shows a certain agreement with the observation of GIE at KAK in the Kanto area. We found disagreement with GIE observed at MMB and KNY. The disagreement may come from the inaccurate conductivity

model. By incorporating data obtained by Magneto-Telluric survey, the disagreement will be settled in the near future. The main Japanese islands are distributed along an arc. As discussed by Divett et al. (2017), the strongest electric fields develop in the direction perpendicular to the island's main axis. In our result, Figure 4 shows GIE is enhanced when incident electric field is perpendicular with the main axis of the Japanese islands. In addition, Figure 5g shows that the largest GIC flows in a southern part of Japan (stretching northeast-southwest) when E_0 directs southeast. These are consistent with the expectation of Divett et al. (2017).

Using the calculated GIE, we calculated GIC flowing in the 500-kV power grid in Japan. The calculated GIC qualitatively agrees with the two observed GIC time series. We first focus on the result obtained with uniform geoelectric field to investigate the influence of the geometry of the power grid on GIC (Figures 5a–5d). GIC appears to be intensified at the westernmost and easternmost points of the power grid when the EW aligned electric field is imposed on the surface as shown in Figure 5a. The same tendency is found for the NS aligned electric field that results in the intensification of GIC at the northernmost and southernmost points. This result is expected from the equation derived by Lehtinen and Pirjola (1985) and is consistent with the simulation results obtained by, for example, Beggan et al. (2013) and Divett et al. (2017). It is noteworthy that GIC is remarkably intensified at KWZ when the NS aligned electric field is imposed on the surface. It is plausible that KWZ is a counterpart of many substations in the Kanto area being located to the south of KWZ. The Kanto area includes the Greater Tokyo Area in which the total population is approximately 38 million and is the most populous metropolitan area in the world as of today. Many substations are situated in the Greater Tokyo Area to accommodate high demand for electric power. Due to this type of topology of the network, GIC flowing at many substations in the Greater Tokyo Area is concentrated to KWZ. The power line between KWZ and the Kanto area is designed for the ultrahigh voltage of 1,000 kV, so that the conductivity is low in this particular power line. This also results in the remarkably intensified GIC at KWZ. We think that this is a unique situation in comparison with other counties.

Next, we discuss the result obtained with the realistic, inhomogeneous, and the 3-D distribution of the ground conductivity. One immediate influence of the realistic ground conductivity is the intensification of GIC near the coast as pointed out by Beggan et al. (2013). This is understood to the intensification of GIE near the coast where the gradient of the conductivity is large. Ivannikova et al. (2018) calculated GIE in Ireland and pointed out that the coastal effect depends on frequency of the imposed field. In Island of Ireland (which is comparable to the Hokkaido island in Japan in size), the coastal effect spreads inward most at the period of 50 s. Divett et al. (2017) investigated GIC in New Zealand and concluded that the maximum GIC occurs when the incident electric field is perpendicular with the island's main axis. This conclusion is also supported by our simulation result. Again, GIC is abnormally intensified at KWZ in the case of the realistic ground conductivity. GIC is not simply proportional to the local GIE. Topology of the network is supposed to play an important role in the distribution of GIC.

In future research, based on our newly developed method for estimation of GIC, we will search for a current system that results in a large-amplitude GIC in Japan. In addition to the geometry of the power grid, the uneven distribution of the GIE is found to contribute significantly to the GIC in Japan. The localized distribution of the sediment layer could significantly affect the GIE distribution. In particular, our simple assumption that the basement rock has a uniform conductivity should be modified since the spatial variations of crustal and mantle conductivity is not large (several orders). Compilation of regional conductivity structures in Japan is necessary to provide a precise prediction of GIC. We considered only the 500-kV power grid lines in this study. The influence of the 275-kV power grid lines on the overall distribution of GIC will be studied in the future. More realistic values of cable resistances and other circuit characters can of course give a detailed estimation of GIC at each grid.

Appendix A

From (1) and (2), the following wave equation can be derived for free space

$$\nabla^2 \boldsymbol{E} + \mu_0 \epsilon_0 \frac{\partial^2 \boldsymbol{E}}{\partial t^2} = 0. \tag{A1}$$

When the electric and magnetic fields depend only on the z component, (A1) turns into

$$\frac{\partial^2 E_y}{\partial z^2} + \mu_0 \epsilon_0 \frac{\partial^2 E_y}{\partial t^2} = 0. \tag{A2}$$

The left-hand side of (A2) indicates the propagation of the electric field in the z direction. When the electric field propagates downward (negative z component), (A2) yields

$$\frac{\partial E_y}{\partial z} - \sqrt{\mu_0 \epsilon_0} \frac{\partial E_y}{\partial t} = 0. \tag{A3}$$

For the free space between the source current at z_s and the surface of the ground at z_0, we obtain a solution of (A3) as

$$E_y = A \cos\left[k(z - z_s) + \frac{2\pi}{T} t\right], \tag{A4}$$

where k is the wave number, and A is a constant. For the long-period variation of the source current, the wave number k is extremely low ($k \approx 0$), so that the wave length is much longer than the distance between the source altitude and the surface of the ground. Thus, the direction of the incident electric field on the ground at z_0 is basically the same as that of the electric field at z_s. We imposed the source current $j_{s,y}$ at z_s, which gives rise to the temporal variation of the electric field at z_s as

$$\frac{\partial E_y}{\partial t} = -\frac{j_{s,y}}{\epsilon_0}. \tag{A5}$$

Therefore, the incident electric field on the ground at z_0 can be basically regarded to be opposite to that of the source current.

Acknowledgments
The authors wish to express their thanks to Kakioka Magnetic Observatory (http://www.kakioka-jma.go.jp/obsdata/metadata/en), Japan Meteorological Agency, for providing electric and magnetic field data. The sym-H index data were obtained from WDC for geomagnetism, Kyoto. We greatly appreciate Tokyo Electric Power Company on the observation of GIC. This work was supported by MEXT/JSPS KAKENHI grant JP15H05815. This study is also supported by Research Mission 5-3 at RISH, Kyoto University. The simulation data are available at the Web http://space.rish.kyoto-u.ac.jp/paper/2018_GICpaper/. The measurements of GIC at STB and SFJ substations have been conducted under the contract between NICT and the electric company. Please contact Shin-Ichi Watari (watari@nict.go.jp) and Yusuke Ebihara (ebihara@r-ish.kyoto-u.ac.jp) for detailed information about the GIC data.

References

Amante, C., & Eakins, B. W. (2009). ETOPO1 1 arc-minute global relief model: Procedures, data sources and analysis (Tech. Rep. NESDIS NGDC-24). Boulder, CO: National Geophysical Data Center, National Oceanic and Atmospheric Administration (NOAA).

Araki, T. (2014). Historically largest geomagnetic sudden commencement (SC) since 1868. *Earth, Planets and Space*, *66*(1), 164. https://doi.org/10.1186/s40623-014-0164-0

Beggan, C. D. (2015). Sensitivity of geomagnetically induced currents to varying auroral electrojet and conductivity models. *Earth, Planets and Space*, *67*(1), 24. https://doi.org/10.1186/s40623-014-0168-9

Beggan, C. D., Beamish, D., Richards, A., Kelly, G. S., & P. Thomson, A. W. (2013). Prediction of extreme geomagnetically induced currents in the UK high-voltage network. *Space Weather*, *11*, 407–419. https://doi.org/10.1002/swe.20065

Béland, J., & Small, K. (2004). Space weather effects on power transmission systems: The cases of Hydro-Québec and Transpower New Zealand Ltd. In I. A. Daglis (Ed.), *Effects of space weather on technology infrastructure* (pp. 287–299). Dordrecht, Netherlands: Springer. https://doi.org/10.1007/1-4020-2754-015

Berenger, J.-P. (1994). A perfectly matched layer for the absorption of electromagnetic waves. *Journal of Computational Physics*, *114*(2), 185–200. https://doi.org/10.1006/jcph.1994.1159

Blake, S. (2017). Modelling and monitoring geomagnetically induced currents in Ireland. Trinity College Dublin.School of Physics.PHYSICS, 2018. Retrieved from http://hdl.handle.net/2262/82549

Bolduc, L. (2002). GIC observations and studies in the Hydro-Québec power system. *Journal of Atmospheric and Solar-Terrestrial Physics*, *64*(16), 1793–1802. https://doi.org/10.1016/S1364-6826(02)00128-1

Boteler, D. H. (2001). Space weather effects on power systems. In P. Song, H. J. Singer, & G. L. Siscoe (Eds.), *Space weather*, *Geophysical Monograph Series* (Vol. 125, pp. 347–352). Washington, DC: American Geophysical Union. https://doi.org/10.1029/GM125p0353

Boteler, D. H., Shier, R. M., Watanabe, T., & Horita, R. E. (1989). Effects of geomagnetically induced currents in the BC Hydro 500 kV system. *IEEE Transactions on Power Delivery*, *4*(1), 818–823. https://doi.org/10.1109/61.19275

Cagniard, L. (1953). Basic theory of the magneto-telluric method of geophysical prospecting. *Geophysics*, *18*(3), 605–635. https://doi.org/10.1190/1.1437915

Divett, T., Ingham, M., Beggan, C., Richardson, G., Rodger, C. J., Thomson, A. W. P., & Dalzell, M. (2017). Modeling geo-electric fields around New Zealand to explore geomagnetically induced current (GIC) in the South Island's electrical transmission network. *Space Weather*, *15*, 1396–1412. https://doi.org/10.1002/2017SW001697

Fujita, S., Fujii, I., Endo, A., & Tominaga, H. (2018). Numerical modeling of spatial profiles of geomagnetically induced electric field intensity in and around Japan. *Technical Report of the Kakioka Magnetic Observatory*, *15*(1), 35–50.

Gaunt, C. T., & Coetzee, G. (2007). Transformer failures in regions incorrectly considered to have low GIC-risk. *Proceedings of the IEEE Powertech Conference*, *445*, 807–812. https://doi.org/10.1109/PCT.2007.4538419

Goto, T. (2015). Numerical studies of geomagnetically induced electric field on seafloor and near coastal zones incorporated with heterogeneous conductivity distributions. *Earth, Planets and Space*, *67*(1), 193. https://doi.org/10.1186/s40623-015-0356-2

Honkonen, I., Kuvshinov, A., Rastätter, L., & Pulkkinen, A. (2018). Predicting global ground geoelectric field with coupled geospace and three-dimensional geomagnetic induction models. *Space Weather*, *16*, 1028–1041. https://doi.org/10.1029/2018SW001859

Honkura, Y. (1985). Perturbation of induced electric currents by surface conductivity inhomogeneity with special reference to anomalous behavior of short-period geomagnetic variations in the Kanto Plain, Japan. *Journal of Geomagnetism and Geoelectricity*, *37*(6), 627–641. https://doi.org/10.5636/jgg.37.627

Ivannikova, E., Kruglyakov, M., Kuvshinov, A., Rastätter, L., & Pulkkinen, A. (2018). Regional 3-D modeling of ground electromagnetic field due to realistic geomagnetic disturbances. *Space Weather*, *16*, 476–500. https://doi.org/10.1002/2017SW001793

Iyemori, T. (1990). Storm-time magnetospheric currents inferred from mid-latitude geomagnetic field variations. *Journal of Geomagnetism and Geoelectricity*, *42*(11), 1249–1265.

Kamide, Y., & Brekke, A. (1975). Auroral electrojet current density deduced from the Chatanika radar and from the Alaska Meridian Chain of magnetic observatories. *Journal of Geophysical Research*, *80*(4), 587–594. https://doi.org/10.1029/JA080i004p00587

Kappenman, J. G. (1989). Effects of geomagnetic disturbances on power systems. *IEEE Power Engineering Review*, *9*(10), 15–20. https://doi.org/10.1109/MPER.1989.4310295

Kappenman, J. G. (2004). The Evolving Vulnerability of Electric Power Grids. *Space Weather*, *2*, S01004. https://doi.org/10.1029/2003SW000028

Kelbert, A., Balch, C. C., Pulkkinen, A., Egbert, G. D., Love, J. J., Rigler, E. J., & Fujii, I. (2017). Methodology for time-domain estimation of storm time geoelectric fields using the 3-D magnetotelluric response tensors. *Space Weather*, *15*, 874–894. https://doi.org/10.1002/2017SW001594

Kikuchi, T., Lühr, H., Kitamura, T., Saka, O., & Schlegel, K. (1996). Direct penetration of the polar electric field to the equator during a DP 2 event as detected by the auroral and equatorial magnetometer chains and the EISCAT radar. *Journal of Geophysical Research*, *101*(A8), 17,161–17,173. https://doi.org/10.1029/96JA01299

Kobea, A. T., Richmond, A. D., Emery, B. A., Peymirat, C., Lühr, H., Moretto, T., et al. (2000). Electrodynamic coupling of high and low latitudes: Observations on May 27, 1993. *Journal of Geophysical Research*, *105*(A10), 22,979–22,989. https://doi.org/10.1029/2000JA000058

Kuvshinov, A. V. (2008). 3-D global induction in the oceans and solid Earth: Recent progress in modeling magnetic and electric fields from sources of magnetospheric, ionospheric and oceanic origin. *Surveys in Geophysics*, *29*(2), 139–186. https://doi.org/10.1007/s10712-008-9045-z

Laske, G., & Masters, T. G. (1997). A global digital map of sediment thickness. *Eos, Transactions of the American Geophysical Union*, *78*(46), 483.

Lehtinen, M., & Pirjola, R. (1985). Currents produced in earthed conductor networks by geomagnetically-induced electric fields. *Annales Geophysicae*, *3*(4), 479–484.

Liu, C., Li, Y., & Pirjola, R. (2014). Observations and modeling of GIC in the Chinese large-scale high-voltage power networks. *Journal of Space Weather and Space Climate*, *4*, 3–9. https://doi.org/10.1051/swsc/2013057

Liu, C.-M., Liu, L.-G., Pirjola, R., & Wang, Z.-Z. (2009). Calculation of geomagnetically induced currents in mid- to low-latitude power grids based on the plane wave method: A preliminary case study. *Space Weather*, *7*, S04005. https://doi.org/10.1029/2008SW000439

Liu, L. Y., & Xie, X. W. (2005). Analysis of increase of noise of 500-kV transformer. *High Voltage Engineering*, *31*(4), 85–87.

Mackie, R. L., Smith, J. T., & Madden, T. R. (1994). Three-dimensional electromagnetic modeling using finite difference equations: The magnetotelluric example. *Radio Science*, *29*, 923–935. https://doi.org/10.1029/94RS00326

Marshall, R. A., Kelly, A., Van Der Walt, T., Honecker, A., Ong, C., Mikkelsen, D., et al. (2017). Modeling geomagnetic induced currents in Australian power networks. *Space Weather*, *15*, 895–916. https://doi.org/10.1002/2017SW001613

McKay, A. J., & Whaler, K. A. (2006). The electric field in northern England and southern Scotland: Implications for geomagnetically induced currents. *Geophysical Journal International*, *167*, 613–625. https://doi.org/10.1111/j.1365-246X.2006.03128.x

Minamoto, Y. (2013). Availability and access to data from Kakioka Magnetic Observatory, Japan. *Data Science Journal*, *12*, G30–G35. https://doi.org/10.2481/dsj. G-040

Ministry of Economy, Trade and Industry of Japan (2015). FY 2014 report on specification researches of standard technologies of electrical power equipments, summarized by the Institute of Applied Energy (written in Japanese, translated by S.N.). Retrieved from http://www.meti.go.jp/meti_lib/report/2015fy/000095.pdf (accessed on January 6, 2018).

Nishida, A. (1968). Geomagnetic *Dp* 2 fluctuations and associated magnetospheric phenomena. *Journal of Geophysical Research*, *73*(5), 1795–1803. https://doi.org/10.1029/JA073i005p01795

Parkinson, W. D., & Jones, F. W. (1979). The geomagnetic coast effect. *Reviews of Geophysics*, *17*(8), 1999–2015. https://doi.org/10.1029/RG017i008p01999

Pulkkinen, A., Bernabeu, E., Eichner, J., Beggan, C., & Thomson, A. W. P. (2012). Generation of 100-year geomagnetically induced current scenarios. *Space Weather*, *10*, S04003. https://doi.org/10.1029/2011SW000750

Pulkkinen, A., Kataoka, R., Watari, S., & Ichiki, M. (2010). Modeling geomagnetically induced currents in Hokkaido, Japan. *Advances in Space Research*, *46*(9), 1087–1093. https://doi.org/10.1016/j.asr.2010.05.024

Pulkkinen, A., Lindahl, S., Viljanen, A., & Pirjola, R. (2005). Geomagnetic storm of 29–31 October 2003: Geomagnetically induced currents and their relation to problems in the Swedish high-voltage power transmission system. *Space Weather*, *3*, S08C03. https://doi.org/10.1029/2004SW000123

Pulkkinen, A., Pirjola, R., & Viljanen, A. (2008). Statistics of extreme geomagnetically induced current events. *Space Weather*, *6*, S07001. https://doi.org/10.1029/2008SW000388

Püthe, C., Manoj, C., & Kuvshinov, A. (2014). Reproducing electric field observations during magnetic storms by means of rigorous 3-D modelling and distortion matrix co-estimation. *Earth, Planets and Space*, *66*(1), 162. https://doi.org/10.1186/s40623-014-0162-2

Taflove, A. (1980). Application of the finite-difference time-domain method to sinusoidal steady state electromagnetic penetration problems. *IEEE Transactions on Electromagnetic Compatibility*, *22*(3), 191–202. https://doi.org/10.1109/TEMC.1980.303879

Takasu, N., Oshi, T., Miyashita, F., Saito, S., & Fujiwara, Y. (1994). An experimental analysis of excitation of transformers by geomagnetically induced currents. *IEEE Transactions on Power Delivery*, *9*(2), 1173–1179.

Thomson, A., Reay, S., & Dawson, E. (2011). Quantifying extreme behavior in geomagnetic activity. *Space Weather*, *9*, S10001. https://doi.org/10.1029/2011SW000696

Tsurutani, B. T., Gonzalez, W. D., Lakhina, G. S., & Alex, S. (2003). The extreme magnetic storm of 1–2 September 1859. *Journal of Geophysical Research*, *108*(A7), 1268. https://doi.org/10.1029/2002JA009504

Tsurutani, B. T., Gonzalez, W. D., Lakhina, G. S., & Alex, S. (2005). Reply to comment by S.-I. Akasofu and Y. Kamide on "The extreme magnetic storm of 1–2 September 1859". *Journal of Geophysical Research*, *110*, A09227. https://doi.org/10.1029/2005JA011121

Uyeshima, M., & Schultz, A. (2000). Geoelectromagnetic induction in a heterogeneous sphere: A new three-dimensional forward solver using a conservative staggered-grid finite difference method. *Geophysical Journal International*, *140*(3), 636–650.

Viljanen, A., & Pirjola, R. (1989). Statistics on geomagnetically-induced currents in the Finnish 400kV power system based on recordings of geomagnetic variations. *Journal of Geomagnetism and Geoelectricity*, *41*(4), 411–420.

Walker, G., & Wong, Y. (1993). Ionospheric effects observed throughout East Asia of the large magnetic storm of 13–15 March 1989. *Journal of Atmospheric and Terrestrial Physics*, *55*(7), 995–1008. https://doi.org/10.1016/0021-9169(93)90093-E

Watari, S., Kunitake, M., & Watanabe, T. (2001). The Bastille day (14 July 2000) event in historical large Sun-Earth connection events. *Solar Physics*, *204*, 423–436.

Weigel, R. S., & Baker, D. N. (2003). Probability distribution invariance of 1-minute auroral-zone geomagnetic field fluctuations. *Geophysical Research Letters*, *30*(23), 2193. https://doi.org/10.1029/2003GL018470

Wik, M., Viljanen, A., Pirjola, R., Pulkk inen, A., Wintoft, P., & Lundstedt, H. (2008). Calculation of geomagnetically induced currents in the400 kV power grid in southern Sweden. *Space Weather*, *6*, S07005. https://doi.org/10.1029/2007SW000343

Yee, K. (1966). Numerical solution of initial boundary value problems involving Maxwell's equations in isotropic media. *IEEE Transactions on Antennas and Propagation*, *14*(3), 302–307.

Yokoyama, N., Kamide, Y., & Miyaoka, H. (1998). The size of the auroral belt during magnetic storms. *Annales Geophysicae*, *16*(5), 566–573. https://doi.org/10.1007/s00585-998-0566-z